

CrossMark  
click for updatesCite this: *J. Mater. Chem. A*, 2016, 4, 13859

## Sulfur to oxygen substitution in BiOCuSe and its effect on the thermoelectric properties

Mi-Kyung Han,<sup>a</sup> Ying-Shi Jin,<sup>a</sup> Byung Kyu Yu,<sup>a</sup> Woongjin Choi,<sup>b</sup> Tae-Soo You<sup>b</sup> and Sung-Jin Kim<sup>\*a</sup>

The effects of S doping at the oxygen site on the thermoelectric properties of BiOCuSe have been investigated. The partial substitution of S ions at the O sites of BiOCuSe was achieved by sulfurization using CS<sub>2</sub> gas. Analysis of the powder X-ray diffraction data indicates that the ZrCuSiAs structure of BiOCuSe is retained after sulfurization. Substitution of O with S leads to an increase in the lattice parameters and a decrease in the band gap. The electrical conductivity rises due to the increase of the electronic contribution with doping. S-doped BiOCuSe materials behave as a p-type semiconductor. The thermoelectric properties of S-doped BiOCuSe materials can be understood through the analysis of the electronic band structure and the density of states close to the Fermi level. The substitution of O sites with S provides possible directions toward the enhancement of the thermoelectric figure of merit of oxide materials with low electrical conductivity.

Received 24th May 2016  
Accepted 8th August 2016

DOI: 10.1039/c6ta04310k

www.rsc.org/MaterialsA

### Introduction

Thermionic conversion of heat energy into electrical energy is a very promising technology for waste heat recovery.<sup>1,2</sup> The key issue in thermoelectric research is to develop materials with a high thermoelectric figure of merit,  $ZT = \sigma S^2 T / \kappa$ , where  $S$  is the Seebeck coefficient (or thermopower),  $\sigma$  is the electrical conductivity,  $\kappa$  is the thermal conductivity, and  $T$  is the temperature in Kelvin.<sup>3,4</sup>

Thermoelectric oxides have been widely investigated over the past decades owing to their nontoxicity, low cost, and thermal and chemical stability in air. However, their  $ZT$  values still remain low mainly because of their low electrical conductivity with a relatively high thermal conductivity.<sup>5,6</sup> Recently, layered BiOCuSe comprising alternating insulating (Bi<sub>2</sub>O<sub>2</sub>)<sup>2+</sup> oxide layers and conductive (Cu<sub>2</sub>Se<sub>2</sub>)<sup>2-</sup> layers has attracted considerable interest owing to its intrinsically low thermal conductivity, namely, the thermal conductivities (0.3–0.5 W m<sup>-1</sup> K<sup>-1</sup>).<sup>7–9,12,13</sup> Taking advantage of this merit of BiOCuSe, further enhancement of  $ZT$  can be achieved by improving its electrical transport properties by controlling carriers. For examples, high  $ZT$  values have been obtained by increasing the carrier concentration through doping with various metal elements, or by improving the carrier mobility through modulation doping. In particular, the electrical transport properties ( $S^2\sigma$ ) were enhanced by the substitution of various hole dopants such as M<sup>+</sup> or M<sup>2+</sup> (Na, Mg,

Ca, Sr, Ba, and Pb) for the Bi site in the insulating (Bi<sub>2</sub>O<sub>2</sub>)<sup>2+</sup> layer or A<sup>1+</sup> or A<sup>2+</sup> (Ag, Cd, and Zn) for the Cu site in the conductive (Cu<sub>2</sub>Se<sub>2</sub>)<sup>2-</sup> layer, thus enhancing  $ZT$  (e.g.,  $ZT \sim 1.2$  for Bi<sub>0.94</sub>Pb<sub>0.06</sub>OCuSe at 900 K;  $ZT \sim 0.9$  for Bi<sub>0.985</sub>Na<sub>0.015</sub>CuSeO;  $ZT \sim 0.8$  for BiCu<sub>0.975</sub>SeO;  $ZT \sim 1.5$  for Bi<sub>0.88</sub>Ca<sub>0.06</sub>Pb<sub>0.06</sub>CuSeO).<sup>10–21</sup> Moreover, Cu-deficient or dual vacancies in Cu and Bi sites are also known to act as hole dopants enhancing their thermoelectric performance ( $ZT \sim 0.81$  for BiCu<sub>0.975</sub>SeO;  $ZT \sim 0.84$  for Bi<sub>0.975</sub>Cu<sub>0.975</sub>SeO).<sup>22,23</sup> Texturing through hot-forging is used for increasing the carrier mobility along the  $ab$ -plane, thus enhancing the electrical conductivity and resulting in a record  $ZT$  of  $\sim 1.4$  at 923 K for Bi<sub>0.875</sub>Ba<sub>0.125</sub>CuSeO.<sup>23</sup> Alternatively, the electronic band structure can be tuned by the substitution of Se in the conductive [Cu<sub>2</sub>Se<sub>2</sub>]<sup>2-</sup> layer with Te or S. For example, the band gap is  $\sim 1.1$ , 0.8, and 0.4 eV for BiOCuS, BiOCuSe, and BiOCuTe analogs, respectively.<sup>24</sup> By the substitution of Se with Te, electrical conductivity was significantly improved, and thus a high  $ZT$  of 0.71 at 923 K was achieved for BiCuSe<sub>0.94</sub>Te<sub>0.06</sub>O.<sup>25</sup> However, the substitution of Se with S decreases the electrical conductivity, because of the increasing ionic character of both the intralayer and interlayer bonding.<sup>26</sup> To the best of our knowledge, the effect of the substitution of the O site in BiOCuSe on the thermoelectric performances of bulk BiOCuSe-based samples has not been evaluated to date.

The purpose of this study was to improve the electrical properties of this material by decreasing the ionic character of the (Bi<sub>2</sub>O<sub>2</sub>)<sup>2+</sup> oxide layer by the substitution of the oxygen site with sulfur. The effect of the substitution of oxygen with sulfur on the thermoelectric properties and the electronic structure was investigated. The experimental study has been combined with  $ab$  initio density functional theory (DFT) calculations to

<sup>a</sup>Department of Chemistry and Nano Science, Ewha Womans University, Seoul, 120-750, Korea. E-mail: sjkim@ewha.ac.kr

<sup>b</sup>Department of Chemistry, Chungbuk National University, Cheongju, Chungbuk 28644, Korea

explain the electrical behaviour of these materials. In this study, we report the synthesis, microstructure, and thermoelectric properties of the S-doped BiOCuSe.

## Experimental

### Sample preparation

BiOCuSe samples with a total mass of *ca.* 10 g were synthesized by mixing appropriate stoichiometric ratios of high purity starting materials, namely Bi<sub>2</sub>O<sub>3</sub>, Cu and Se (>99.99% purity). The corresponding materials were hand-mixed using a pestle and a mortar and sealed in evacuated fused silica tubes (10 mm diameter, 1 mm wall thickness) under a residual pressure of  $\sim 10^{-4}$  Torr. The sealed tubes were heated in two successive steps: (1) to 300 °C over 3 h and held there for 3 h and (2) to 700 °C over 4 h and held there for 12 h. The temperature was slowly cooled down to room temperature over 10 h.

S-doped BiOCuSe samples were prepared by the sulfurization of BiOCuSe powders. BiOCuSe (5 g) was placed on a silica boat and inserted into a silica-glass tube. After flushing with Ar gas at room temperature, the boat was heated to various temperatures such as 200, 250, 300, 450, 650, and 800 °C, and then the CS<sub>2</sub> gas was introduced into the reactor by passing Ar carrier gas through a bubbler containing CS<sub>2</sub>. The sulfurization experiment was carried out for 6 h.

### Fabrication of nanostructured bulk materials by spark plasma sintering (SPS)

The S-doped BiOCuSe powder was consolidated using an SPS machine (SPS-211Lx, Fuji Electronic Industrial Co., LTD, Japan) to obtain dense bulks. Typically,  $\sim 2$  g of the powder was loaded in a graphite die with an inner diameter of 10 mm. To determine a suitable sintering temperature, the powder was heated to several different temperatures (*e.g.*, 500, 600, and 650 °C) at a heating rate of 100 °C min<sup>-1</sup> under the conditions of vacuum and at a uniaxial pressure of  $\sim 50$  MPa, and the holding time was 5 min at the sintering temperature. After sintering, disk-shaped pellets with a diameter of 10 mm and thickness of 2–3 mm were obtained.

### Characterization of materials

The crystal structure of the obtained products was confirmed by the powder X-ray diffraction (XRD), recorded using a Rigaku X-ray diffractometer using Cu K $\alpha_1$  radiation ( $\lambda = 0.15418$  nm) at 30 mA and 40 kV. The lattice parameters were obtained by least squares refinement of data in the  $2\theta$  range 20–70° with the aid of a Rietveld refinement program.<sup>27</sup> The orientation factor, *F*, was determined from the XRD pattern by the Lotgering method. The morphologies of the as-prepared samples were investigated by field-emission scanning electron microscopy (FE-SEM, JEOL JSM-5800F) and high-resolution transmission electron microscopy (HRTEM, JEOL JEM-2100F). To probe the optical energy band gap of the S-doped BiOCuSe, room temperature optical diffuse reflectance measurements were performed using a Nicolet 6700 FTIR spectrometer. The spectra were monitored in the UV-Vis region (2600–200 cm<sup>-1</sup>). Absorption data were

calculated from the reflectance data using the Kubelka–Munk function.<sup>28</sup> The optical bandgaps were derived from absorption *versus E* (eV) plots.

Thermal conductivity was determined by combining thermal diffusivity (*D*), specific heat (*C<sub>p</sub>*) and sample density ( $\rho$ ) according to  $\kappa_{\text{tot}} = D \times C_p \times \rho$ . To measure the thermal diffusivity, the samples were cut into disks of  $\sim 10$  mm diameter and 2 mm thickness along the direction parallel to the SPS pressing direction. Thermal diffusivity and specific heat were determined by the flash diffusivity-heat capacity method using a NETZSCH LFA 457 MicroFlash™ instrument. A reference material, Pyroceram, of known heat capacity was used as a reference for the determination of the specific heat of the sample. The  $\rho$  was measured using the sample's geometry and mass. The measured density of the S-doped BiOCuSe bulk sample was 8.57 g cm<sup>-3</sup>, representing 96% of the theoretical density of the pristine BiOCuSe. For the measurements of electrical properties, the samples were cut into rectangles of  $\sim 3 \times 3 \times 8$  mm<sup>3</sup> along the directions perpendicular to the SPS pressing direction to ensure that all TE properties are measured in the same direction. The electrical conductivity and Seebeck coefficient were measured simultaneously under a helium atmosphere from room temperature to  $\sim 700$  K using a ULVAC-RIKO ZEM-3. The Seebeck coefficients were measured three times with different temperature gradients between 10 and 30 K at each temperature step.

### Electronic structure calculation

A series of theoretical investigations have been conducted by using the Stuttgart TB-LMTO47 program<sup>29–33</sup> with the atomic sphere approximation (ASA) method for two structural models with idealized compositions of “BiOCuSe” and “BiSCuSe”. The local density approximation (LDA) was applied for exchange and correlation.<sup>29–33</sup> A scalar relativistic approximation was taken to treat all the relativistic effects, except spin-orbit coupling. In the ASA method, the space was filled with overlapping Wigner–Seitz (WS) atomic spheres.<sup>29–33</sup> The symmetry of the potential inside each WS sphere was considered spherical, and a combined correction was used to take into account the overlapping part.<sup>34</sup> The radii of the WS sphere were obtained by requiring the overlapping potential be the best possible approximation to the full potential and were determined by an automatic procedure.<sup>34</sup> This overlap should not be too large, because the error in kinetic energy introduced by the combined correction was proportional to the fourth power of the relative sphere overlap. The used WS radii are listed as follows: Bi = 1.656 Å, O = 1.113 Å, Cu = 1.426 Å and Se = 1.606 Å for BiOCuSe; and Bi = 1.582 Å, S = 1.371 Å, Cu = 1.511 Å, and Se = 1.701 Å for BiSCuSe. The basis sets included 6s, 6p, 6d, and 5f orbitals for Bi; 3s, 2p, and 3d orbitals for O; 3s, 3p, and 3d orbitals for S; 4s, 4p, and 3d orbitals for Cu; and 4s, 4p, and 4d orbitals for Se. The Bi 6d and 5f; O 3s and 3d; S 3d; and Se 4d orbitals were treated by the Löwdin downfolding technique.<sup>35</sup> The *k*-space integration was conducted by the tetrahedron method,<sup>36</sup> and the self-consistent charge density was obtained using 612 and 612 irreducible *k*-points in the Brillouin zone, respectively, for BiOCuSe and BiSCuSe.

## Results and discussion

To determine a suitable sulfurization temperature, the pristine sample was sulfurized with CS<sub>2</sub> gas at temperatures between 200 °C and 900 °C. Fig. 1 shows the room temperature XRD patterns of S-doped BiOCuSe formed by the sulfurization of pristine BiOCuSe at different temperatures. All the peaks of the sulfurized products were indexed to the characteristic peaks of BiOCuSe (PDF#45-0296) with a ZrSiCuAs-type structure.<sup>37</sup> According to the XRD patterns, the BiOCuSe structure was maintained in the products sulfurized only at lower than 300 °C, as shown in Fig. 1. In contrast, in the product sulfurized at a temperature of 400 °C or higher, the diffraction intensities of the BiOCuSe structure decreased, and the diffraction peaks of the Bi<sub>3</sub>Se<sub>4</sub> phase appeared. BiOCuSe, Bi<sub>2</sub>S<sub>3</sub>, Cu<sub>2-x</sub>S, and Bi<sub>3</sub>Se<sub>4</sub> were detected from the products reacted at 650 °C, and only Bi<sub>3</sub>Se<sub>4</sub> was detected from the sample sulfurized at 900 °C. Therefore, the sulfurization of pristine BiOCuSe was carried out at 250 °C for the preparation of S-doped samples for the TE measurements. As shown in Fig. 1a, the relative intensity of (00 $l$ ) peaks indicated by the red boxes increased as the temperature increased. The  $ab$  orientation degrees for the (00 $l$ ) crystal planes of the pristine and S-doped sample termed as  $F_{(00l)}$  calculated with the Lotgering method were 0.11 and 0.63 for the samples with a sulfurization temperature of 250 and 300 °C, respectively, indicating that the crystals are preferentially oriented in the  $ab$ -plane.<sup>38</sup> The texturization of the sample would intensify the mobility of electrons, thus increasing the electrical conductivity of the sample. Experimentally, the carrier mobility was slightly increased from 22 to 28 cm<sup>2</sup> V<sup>-1</sup> s<sup>-1</sup> after the sulfurization. The shift of the peaks in the diffraction patterns is observed, indicating that the lattice constant of S-doped BiOCuSe increases with sulfurization temperature, as shown in Fig. 1b. The lattice parameters obtained using the Rietveld refinement of the XRD patterns are plotted in Fig. 1c.

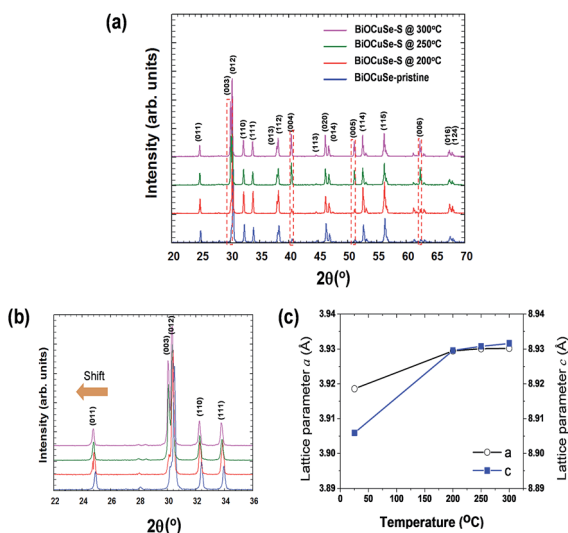


Fig. 1 (a and b) XRD patterns; (c) lattice parameters of BiOCuSe and S-doped BiOCuSe prepared at three different temperatures (200, 250, and 300 °C).

The lattice parameters of the pristine BiOCuSe are  $a = 3.911(1)$  Å and  $c = 8.893(1)$  Å. They are consistent with the values previously reported in the literature.<sup>37</sup> Both lattice parameters  $a$  and  $c$  increase slightly with increasing sulfurization temperature, which is related to the larger S<sup>2-</sup> ions doped in O<sup>2-</sup> sites. In other words, considering that the radius of S<sup>2-</sup> ions (1.84 Å) is much larger than that of O<sup>2-</sup> ions (1.38 Å), the possible explanation for the result is that the larger S<sup>2-</sup> ions probably enter the O<sup>2-</sup> site without disturbing the crystalline structure. This result shows that the sulfurization with CS<sub>2</sub> is an effective way to substitute the O<sup>2-</sup> site with S<sup>2-</sup>. It is worth mentioning that in the conventional solid-state reaction of Bi<sub>2</sub>O<sub>3</sub>, Cu<sub>2</sub>O, Se, and Na<sub>2</sub>S, sulfur is only substituted for the selenium sites forming BiOCuSe<sub>1-x</sub>S<sub>x</sub>, thus decreasing the lattice parameter,<sup>26</sup> whereas by sulfurization with CS<sub>2</sub> gas, S<sup>2-</sup> ions preferentially substitute the O<sup>2-</sup>, not the Se<sup>2-</sup>, forming BiO<sub>1-x</sub>S<sub>x</sub>CuSe.

In addition to the lattice expansion, several changes in the structural parameters were detected upon sulfur doping by tunneling electron microscopy (TEM) and scanning electron microscopy (SEM). Fig. 2a and b display typical high-resolution TEM images of the BiOCuSe before and after the sulfurization. Slight lattice expansion was also detected in the high-resolution TEM image. The inset of Fig. 2a and b shows an electron diffraction pattern, which is consistent with the layer structure feature of BiOCuSe showing the (100) plane. No split Bragg spots were observed, which further confirmed that S<sup>2-</sup> was incorporated into the BiOCuSe lattice as a homogeneous solid solution phase. Fig. 2c and d exhibit the SEM morphologies of the layered BiOCuSe before and after the sulfurization, indicating that the grain sizes of the S-doped BiOCuSe sample are random and similar to that of the pristine one.

The distribution of elements Bi, Cu, Se, S, and O for the S-doped BiOCuSe examined by EDS mapping indicates that all the elements are homogeneously distributed throughout the sample, as shown in Fig. 3a. The EDS spectrum images taken from the pristine BiOCuSe and S-doped BiOCuSe are shown in

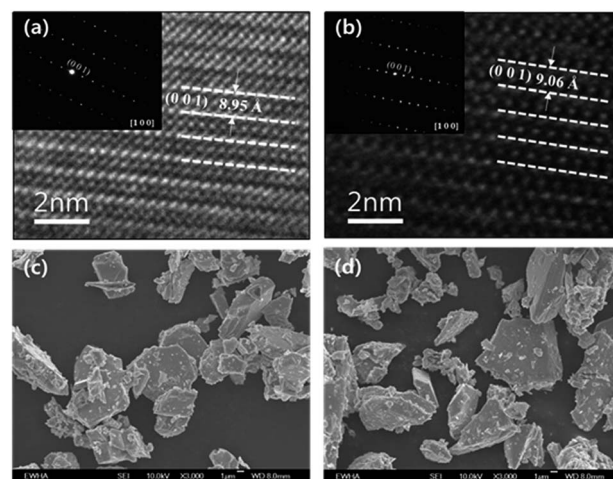


Fig. 2 (a and b) TEM image with the inset of the FFT pattern and SAED pattern. (c and d) SEM micrographs of the pristine BiOCuSe and S-doped BiOCuSe, respectively.

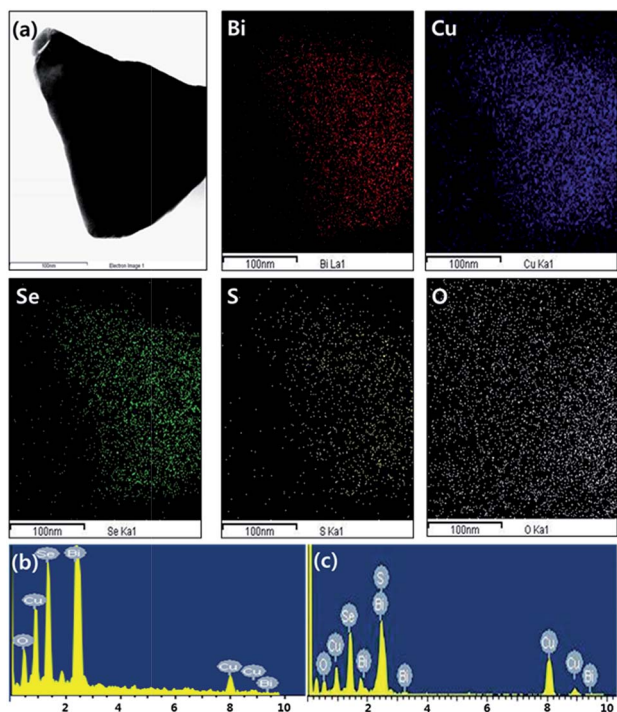


Fig. 3 (a) Element distributions determined by EDS mapping for S-doped BiOCuSe; (b) and (c) the EDX spectrum of the pristine BiOCuSe and S-doped BiOCuSe, respectively.

Fig. 3b and c, respectively. The compositions measured by EDS approximately matched with the stoichiometry, and the S-dopant was indeed present in the samples, although its concentration was somewhat lower. The atomic ratio of S-doped BiOCuSe is Bi : S : Cu : Se = 1 : 0.028(15) : 0.96(4) : 0.94(6), which is close to the value of the pristine BiOCuSe (Bi : S : Cu : Se = 1 : 0.0 : 1.03(2) : 1.06(7)). Although there are some deviations because of the thermal evaporation during the sulfurization in the Ar flow, it still provides indirect evidence for checking the elements and compositions. The presence and oxidation state of S were also confirmed by X-ray photoemission spectroscopy (XPS) analysis. Fig. 4 shows the detailed XPS scans of the Bi and S binding energies of the S-doped BiOCuSe. The survey spectrum in Fig. 4a clearly demonstrates that the sample is composed of Bi, Cu, O, Se, and S elements. The binding energies (Fig. 4b) of 158.3 eV for Bi  $4f_{7/2}$  and 163.6 eV for Bi  $4f_{5/2}$  indicate a trivalent oxidation state for bismuth. Fig. 4c shows the binding energies of S  $2p_{3/2}$  and S  $2p_{1/2}$  peaks in the sample,

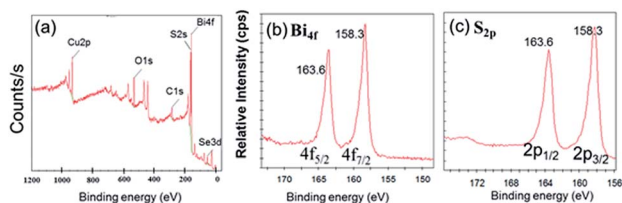


Fig. 4 XPS analysis spectra (a) low-resolution survey scan, (b) Bi 4f core level spectrum, and (c) S 2p core level spectrum from the S-doped BiOCuSe sample.

respectively, located at 158.3 and 163.6 eV, indicating that  $S^{2-}$  exists in the S-doped BiOCuSe sample.

The bandgap of this material can be tuned by the substitution of selenium or oxygen sites with sulfur. It has been shown that the bandgap increases from 0.8 eV to 1.1 eV, when Se sites are completely substituted by S atoms forming BiOCuS.<sup>26</sup> Fig. 5 shows the diffused reflectance spectra converted to absorbance data using the Kubelka–Munk relation:<sup>28</sup>  $\alpha/S = (1 - R)^2/2R$ , where  $R$  is the reflectance and  $\alpha$  and  $S$  are the absorption and scattering coefficients, respectively. The derived bandgap of BiOCuSe is 0.80 eV, which is consistent with the values reported in the literature for this compound.<sup>26</sup> The bandgap of S-doped BiOCuSe slightly shifted towards a lower value, indicating that the S preferentially substituted in the O site, rather than in the Se sites.

A series of comprehensive theoretical calculations were conducted for the two compounds with idealized compositions of “BiOCuSe” and “BiSCuSe” by using the TB-LMTO-ASA method to investigate the effect of the S substitution for the O site on the electronic structures and chemical bonding. Detailed crystallographic data including the space group and the lattice parameters of BiOCuSe for the theoretical approaches were extracted from the PXRD refinements. The structural model for BiSCuSe is isotopic with the BiOCuSe structure designed with slightly increased lattice parameters according to the relatively larger ionic size of  $S^{2-}$  than  $O^{2-}$  (1.84 vs. 1.38 Å, respectively). First, two DOS curves of each structure are displayed and compared in Fig. 6a and b. Both the curves display overall orbital mixings of four components over the entire energy window. The valence band region in BiSCuSe (Fig. 6b) can be roughly divided into three sections: (1) the region between  $-14.5$  and  $-10$  eV shows major contributions from Cu 4s and Se 4s with minor contributions from Bi 6s and S 3s, (2) the region between  $-10$  and  $-7$  eV displays major contributions from Bi 6p and S 3p, and (3) the large region between  $-7$  and 0 eV contains dominant contributions from Cu 3d and Se 4p with small contributions from Bi 6p and S 3p as well. In particular, the s and the p orbitals from Bi and S are largely spread over the entire valence band down to the very low energy region (*ca.*  $-20$  eV) unlike that in BiOCuSe (Fig. 6a). As a consequence, the

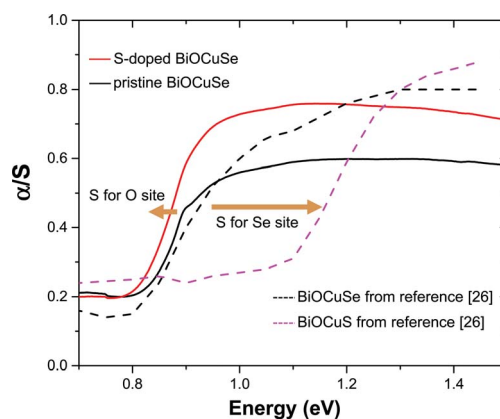


Fig. 5 UV-Vis spectroscopy for BiOCuSe and S-doped BiOCuSe, compared to the previous report.

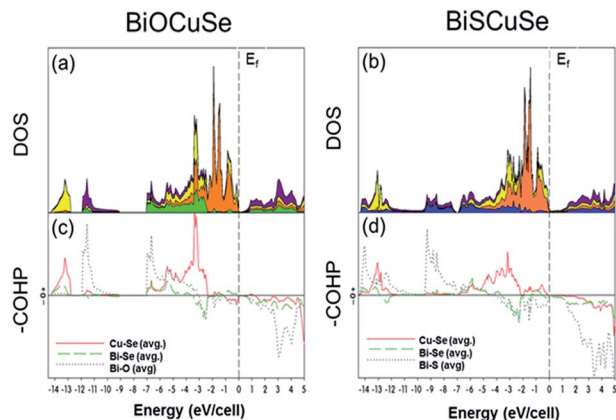


Fig. 6 DOS and COHP curves for BiOCuSe (left; (a) and (c)) and BiSCuSe (right; (b) and (d)). Total DOS (black-bold line), Bi PDOS (purple region), O (left) or S (right) PDOS (green or blue region, respectively), Cu (orange region) and Se (yellow region). COHP curves represent the averaged Cu–Se (red bold line), Bi–Se (green dashed line), and Bi–O (left) or Bi–S (right) (grey dot line) interactions. EF (dashed vertical line) is the energetic reference (0 eV).

contribution of S 3p orbitals to the range between  $-7$  and  $0$  eV is significantly reduced in BiSCuSe as compared to that in BiOCuSe.

Interestingly, the most distinctive difference between the two DOS curves is that a small bandgap observed in BiOCuSe eventually disappeared in BiSCuSe, because of some orbitals flowing out from the valence band and slightly covering the bandgap region. The rationale for this phenomenon should be attributed to the relatively smaller electronegativity of S than that of O (2.58 for S vs. 3.44 for O; Pauling scale), resulting in the less pronounced electron transfer from Bi to S in the two-dimensional  $\frac{2}{3}[\text{Bi}_2\text{S}_2]^{2+}$  layer. The TB-LMTO calculation is known to underestimate the bandgap size. In other words, a theoretically calculated bandgap size obtained by using the TB-LMTO method is usually smaller than an experimentally measured bandgap size. Therefore, we should pay more attention to the relative size comparison between the two calculated bandgaps for two structural models rather than the actual bandgap size comparison between the calculated and the experimentally measured values. Then, the relative sizes of two bandgaps obtained from our theoretical calculation show the same trend as the experimentally measured optical bandgaps of 0.82 and 0.80 eV for BiOCuSe and BiSCuSe, respectively.

Finally, according to COHP curves (Fig. 6c and d) and  $-i\text{COHP}$  values shown in Table 1, the Bi–S  $i\text{COHP}$  value in BiSCuSe is much smaller than that of the Bi–O in BiOCuSe despite the slightly increased bond distance. However, other two  $i\text{COHP}$  values in BiSCuSe are slightly higher than that in BiOCuSe, as can surely be expected from the elongated bond distances. This relatively smaller  $i\text{COHP}$  value of the Bi–S interaction indicates that the Bi–S interaction in BiSCuSe becomes much stronger than the Bi–O interaction in BiOCuSe, because of the  $\text{S}^{2-}$  substitution for  $\text{O}^{2-}$ , and it provides a rationale for the enhanced electrical conductivity. Recently Xu *et al.* showed the charge transfer between the oxide layer and the

Table 1 Selected bond distances (Å) and  $i\text{COHP}$  values for BiOCuSe and BiSCuSe

Atomic pair	BiOCuSe		BiSCuSe	
	Distance	$i\text{COHP}$	Distance	$i\text{COHP}$
Bi–Pn <sup>a</sup>	2.323	−1.178	2.330	−2.173
Cu–Se	2.527	−1.428	2.535	−1.199
Bi···Se (interlayer)	3.190	−0.192	3.200	−0.170

<sup>a</sup> Pn = O and S for BiOCuSe and BiSCuSe, respectively.

selenide layer in a Cu-deficient BiOCuSe system.<sup>39</sup> Considering the  $i\text{COHP}$  value, the hybridization between Bi and Se cannot be neglected, therefore expecting the interlayer charge transfer/redistribution.

To examine the effect of the SPS conditions on the powder densification, the samples were sintered at between 500 and 650 °C. The relative density increases with the increase of SPS temperature. The bulk density was measured to be 76.2%, 95.0%, and 96.3% of the theoretical density in the sample SPS at 500, 600, and 650 °C, respectively. Fig. 7 shows the thermoelectric properties as a function of temperature for S-doped BiOCuSe and the pristine samples. As shown in Fig. 7a, S-doped BiOCuSe exhibits higher electrical conductivity than the pristine BiOCuSe over the entire temperature range and a semi-conducting electrical transport behaviour. This result indicates that S doping can effectively enhance the electrical conductivity of BiOCuSe. The possible origin of the enhanced electrical conductivity of S-doped BiOCuSe can be presumably explained by the bandgap tuning through S doping, whereas, with the substitution of selenium with sulfur, the electrical conductivity was decreased due to the increase of the ionic character of

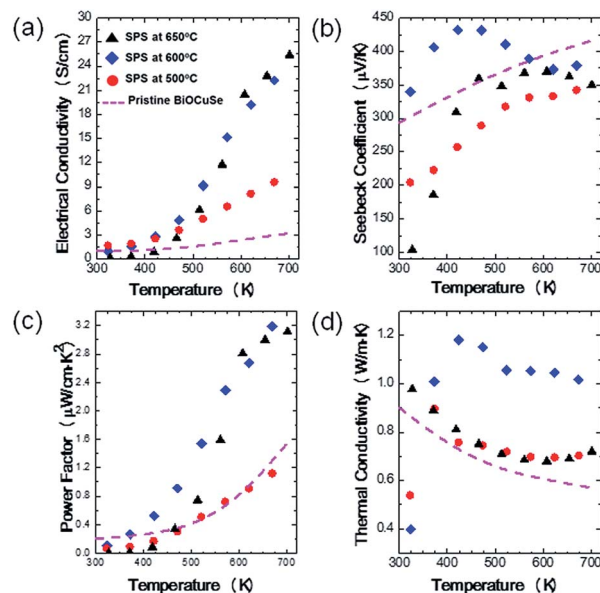


Fig. 7 Temperature dependence of the electrical transport properties of S-doped BiOCuSe prepared by SPS at different sintering temperatures. (a) Electrical conductivity, (b) Seebeck coefficient, (c) power factor, and (d) thermal conductivity.

bonding in this layered material when increasing the sulfur fraction.<sup>26</sup> Doping with S also slightly affects the Seebeck coefficient of the BiOCuSe system, as shown in Fig. 7b. A positive Seebeck coefficient indicates p-type electrical transport behavior. The magnitude of the Seebeck coefficient of S-doped BiOCuSe initially increases, reaches a maximum, and then decreases slightly with increasing temperature, suggesting a compensation by minor carrier activation because of the small band gap. This behavior is unexpected because of the large bandgap of the pristine BiOCuSe. The Seebeck coefficient was maintained in the range 275–325  $\mu\text{V K}^{-1}$  at 700 K. Because of the enhanced electrical conductivity by S-doping, the power factor is much larger than that of the pristine BiOCuSe sample, as shown in Fig. 7c. Fig. 7d shows the total thermal conductivity as a function of temperature. After S-doping, the total thermal conductivity increased slightly. The total thermal conductivity ( $\kappa_{\text{tot}}$ ) is the sum of two contributions, one from the charge carriers ( $\kappa_{\text{elec.}}$ ) and the other from the lattice vibrations ( $\kappa_{\text{latt.}}$ ), ( $\kappa_{\text{tot}} = \kappa_{\text{elec.}} + \kappa_{\text{latt.}}$ ).<sup>40</sup> Here  $\kappa_{\text{elec.}}$  is expressed by the Wiedemann–Franz law,  $\kappa_{\text{elec.}} = L_0\sigma T$ , where  $L_0$  is the Lorenz number and  $T$  is the absolute temperature. The value of the Lorenz number for BiOCuSe ( $L_0 = 2.45 \times 10^{-8} \text{ W } \Omega \text{ K}^{-2}$ ) is used to estimate  $\kappa_{\text{elec.}}$ . For S-doped BiOCuSe, the electronic contribution is increased with increasing temperature and shows the value around 6% of total thermal conductivity at 700 K. The  $\kappa_{\text{latt.}}$  values of BiOCuSe and S-doped BiOCuSe at 700 K are  $\sim 0.51 \text{ W m}^{-1} \text{ K}^{-1}$  and  $\sim 0.68 \text{ W m}^{-1} \text{ K}^{-1}$ , respectively. Because the mass difference between O and Bi is much larger than that between S and Bi, the resulting mass fluctuation scattering is stronger in the BiOCuSe system. Therefore, less phonon scattering exists in the S-doped BiOCuSe leading to a higher lattice thermal conductivity.

Using the electrical and thermal transport properties, the dimensionless figure of merit ( $ZT$ ) was calculated, as shown in Fig. 8. The  $ZT$  shows an increasing trend with temperature, and a maximum  $ZT$  value of 0.3 was achieved at 700 K for the

S-doped sample and is higher than that of 0.12 at 700 K for the pristine BiOCuSe. The present higher thermoelectric performance originates from higher electrical conductivity through bandgap engineering by S-doping. Therefore, the S doping can improve the thermoelectric properties.

## Conclusions

In this study, S-doped BiOCuSe was prepared by sulfurization using  $\text{CS}_2$  gas in the presence of pure argon. After sulfurization of BiOCuSe, the lattice parameters increased and the bandgap decreased, because of the S substitution on the O sites in the  $(\text{Bi}_2\text{O}_2)^{2+}$  layer. The electronic structure calculation indicates that the electronic structure within the  $(\text{Bi}_2\text{O}_2)^{2+}$  layer was significantly affected by the S substitution. Less pronounced electron transfer from S to Bi was observed. The electrical conductivity increased through the bandgap tuning by the S substitution on the O site, and thus the power factor significantly increased. The  $ZT$  was enhanced from 0.12 for the undoped sample to 0.30 for the S-doped BiOCuSe sample at 700 K. This study provides an effective strategy for further improvement of  $ZT$  in BiOCuSe based oxides.

## Acknowledgements

This research was supported by the Nano-Material Technology Development Program through the National Research Foundation of Korea (NRF) funded by the Ministry of Education, Science and Technology (NRF-2011-0030147) and by the National Research Foundation of Korea (NRF) Grant funded by the Korean Government (MSIP) (NRF-2015R1A5A1036133).

## References

- 1 D. M. Rowe, *CRC Handbook of Thermoelectrics*, CRC press, New York, 1995.
- 2 L. E. Bell, *Science*, 2008, **321**, 1457.
- 3 G. J. Snyder and E. S. Toberer, *Nat. Mater.*, 2008, **7**, 105.
- 4 K. Bisas, J. He, I. D. Blum, C. I. Wu, T. P. Hogan, N. D. Seidman, V. P. Dravid and M. G. Kanatzidis, *Nature*, 2012, **489**, 414.
- 5 G. K. Ren, J. L. Lan, C. C. Zeng, Y. C. Liu, B. Zhan, S. Butt, Y. H. Lin and C. W. Nan, *JOM*, 2015, **67**, 211.
- 6 R. Funahshi, M. Mikami, S. Urata, M. Kitawaki, T. Kouuchi and K. Mizuno, *Meas. Sci. Technol.*, 2005, **16**, 70.
- 7 L.-D. Zhao, D. Berardan, Y. L. Pei, C. Byl, L. Pinsard-Gaudart and N. Dragoë, *Appl. Phys. Lett.*, 2010, **97**, 092118.
- 8 L.-D. Zhao, J. Q. He, D. Berardan, Y. H. Lin, J. F. Li, C. W. Nan and N. Dragoë, *Energy Environ. Sci.*, 2014, **7**, 2900.
- 9 Y. L. Pei, J. He, J. F. Li, F. Li, Q. Liu, W. Pan, C. Barreateau, D. Berardan, N. Dragoë and L.-D. Zhao, *NPG Asia Mater.*, 2013, **5**, e47.
- 10 J. Li, J. Sui, Y. Pei, X. Meng, D. Berardan, N. Dragoë, W. Cai and L.-D. Zhao, *J. Mater. Chem. A*, 2014, **2**, 4903.
- 11 J. Li, J. Sui, C. Barreateau, D. Berardan, N. Dragoë, W. Cai, Y. Pei and L.-D. Zhao, *J. Alloys Compd.*, 2013, **551**, 649.

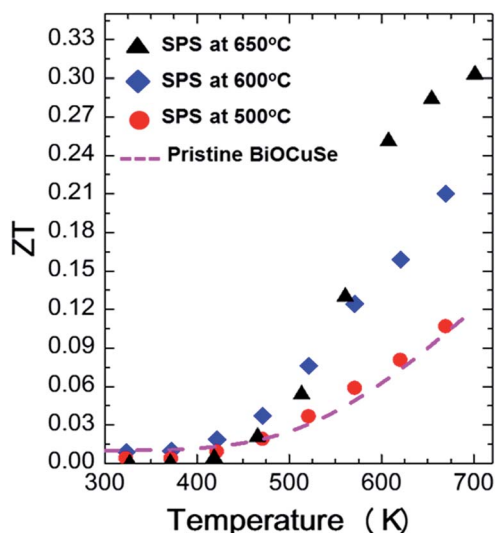


Fig. 8 Figure of merit,  $ZT$ , as a function of temperature for pristine BiOCuSe and S-doped BiOCuSe samples.

- 12 F. Li, T. R. Wei, F. Kang and J. F. Li, *J. Mater. Chem. A*, 2013, **1**, 11942–11949.
- 13 Y. Pei, F. Li, J.-F. Li, Q. Liu, W. Pan, C. Barreateau, D. Béardan, N. Dragoe, J. He and L.-D. Zhao, *NPG Asia Mater.*, 2013, **5**, e47.
- 14 C.-L. Hsiao and X. Qi, *Acta Mater.*, 2016, **102**, 88.
- 15 C. Barreateau, D. Berardan, E. Amzallag, L.-D. Zhao and N. Dragoe, *Chem. Mater.*, 2012, **24**, 3168.
- 16 J. Li, J. Sui, Y. Pei, C. Barreateau, D. Berardan, N. Dragoe, W. Cai, J. He and L.-D. Zhao, *Energy Environ. Sci.*, 2012, **5**, 8543.
- 17 J. L. Lan, Y. C. Liu, B. Zhan, Y. H. Lin, B. Zhang, X. Yuan, W. Zhang, W. Xu and C. W. Nan, *Adv. Mater.*, 2013, **25**, 5086.
- 18 Y. C. Liu, Y. H. Zheng, B. Zhan, K. Chen, S. Butt, B. P. Zhang and Y. H. Lin, *J. Eur. Ceram. Soc.*, 2015, **35**, 845.
- 19 G. Ren, S. Butt, C. Zeng, Y. Liu, B. Zhan, J. Lan, Y. Lin and C. Nan, *J. Electron. Mater.*, 2015, **44**, 1627.
- 20 M. U. Farooq, S. Butt, K. Gao, Y. Zhu, X. Sun, X. Pang, S. U. Khan, F. Mohamed, A. Mahmood, N. Mahmood and W. Xu, *RSC Adv.*, 2016, **6**, 33789.
- 21 Y. Liu, L. Zhao, Y. Zhu, Y. Liu, F. Li, M. Yu, D. Liu, W. Xu, Y. H. Lin and C. W. Nan, *Adv. Energy Mater.*, 2016, **6**, 1502423.
- 22 Y. Liu, L. Zhao, Y. Liu, J. Lan, W. Xu, F. Li, B. P. Zhang, D. Berardan, N. Dragoe, Y. H. Lin, C. W. Nan, J. F. Li and H. Zhu, *J. Am. Chem. Soc.*, 2011, **133**, 20112.
- 23 J. Sui, J. Li, J. He, Y. L. Pei, D. Berardan, H. Wu, N. Dragoe, W. Cai and L.-D. Zhao, *Energy Environ. Sci.*, 2013, **6**, 2916.
- 24 H. Hiramatsu, H. Yanagi, T. Kamiya, K. Ueda, M. Hirano and H. Hosono, *Chem. Mater.*, 2008, **20**, 326.
- 25 Y. Liu, J. Lan, W. Xu, Y. Liu, Y.-L. Pei, B. Cheng, D.-B. Liu, Y.-H. Lin and L.-D. Zhao, *Chem. Commun.*, 2013, **49**, 8075.
- 26 D. Berardan, J. Li, E. Amzallag, S. Mitra, J. Sui, W. Cai and N. Dragoe, *Materials*, 2015, **8**, 1043.
- 27 B. A. Hunter and C. J. Howard, *Rietica*, Australian Nuclear Science and Technology Organization, Menai, Australia, 2000.
- 28 P. Kubelka and F. Munk, *Z. Tech. Phys.*, 1931, **12**, 593.
- 29 O. K. Andersen, *Phys. Rev. B: Condens. Matter Mater. Phys.*, 1975, **12**, 3060.
- 30 O. K. Andersen and O. Jepsen, *Phys. Rev. Lett.*, 1984, **53**, 2571.
- 31 O. K. Andersen, *Phys. Rev. B: Condens. Matter Mater. Phys.*, 1986, **34**, 2439–2449.
- 32 O. Jepsen, A. Burkhardt and O. K. Andersen, *The TB-lmto-asa Program, Version 4.7*, Max-Planck-Institut für Festkörperforschung, Stuttgart, Germany, 1999.
- 33 O. K. Andersen, O. Jepsen, D. Glötzel, F. Bassani, F. Fumi and M. Tosi, *Highlights of Condensed-Matter Theory*, North Holland, New York, 1985.
- 34 O. Jepsen and O. K. Andersen, *Z. Tech. Phys.*, 1995, **97**, 35.
- 35 R. Dronskowski and P. E. Blöchl, *J. Phys. Chem.*, 1993, **97**, 8617.
- 36 P. E. Blöchl, O. Jepsen and O. K. Andersen, *Phys. Rev. B: Condens. Matter Mater. Phys.*, 1994, **49**, 16223.
- 37 A. M. Kusainova, P. S. Berdonosov, L. G. Akselrud, L. N. Kholodkovskaya, V. A. Dolgikh and B. A. Popovkin, *J. Solid State Chem.*, 1994, **112**, 189.
- 38 T. Kobayashi, R. Ogawa, K. Miyazawa and M. Kuwabara, *J. Mater. Res.*, 2002, **17**, 844.
- 39 W. Xu, Y. Liu, L.-D. Zhao, P. An, Y.-H. Lin, A. Marcelli and Z. Wu, *J. Mater. Chem. A*, 2013, **1**, 12154.
- 40 F. J. DiSalvo, *Science*, 1999, **285**, 703.